Electronic-ferry in metal element migration promoting deep activation of NiFe based phosphide for high efficient and stable oxygen evolution reaction

Xiaobing Wang [a],[*],[1], Zhichao Hou [b],[1], Niannian Zhan [a], Zhijie Guo [c],[*], Yong Zhao [a],[*]

[a] Key Lab for Special Functional Materials of Ministry of Education, National & Local Joint Engineering Research Center for High-efficiency Display and Lighting Technology, Collaborative Innovation Center of Nano Functional Materials and Applications, College of Materials, Henan University, Kaifeng 475004, PR China
[b] Key Laboratory of Physics and Technology for Advanced Batteries (Ministry of Education), Jilin Key Engineering Laboratory of New Energy Materials and Technologies, College of Physics, Jilin University, Changchun 130012, PR China
[c] College of Chemistry and Materials Engineering, Bohai University, Jinzhou 121000, China

A R T I C L E I N F O

A B S T R A C T

The design principle of high-efficient water electrolysis catalysis in oxygen evolution reaction (OER) has been primarily focused on the construction of multi-metal active centres. However, the spatial barrier between nonadjacent metal sites restricts the electron transfer, thus limits the activation and stability of active sites for improving the OER performance. Herein, a concept of electronic-ferry strategy by metal element migration in OER reconstruction is adopted to form dynamic electron-bridge between heterogeneous metal ions, which synchronously improves the OER kinetics and the corrosion resistance of metals centres. By designing layered NiCrP@NiFeP with concentration gradient, Cr element stepwise-release from the core part endows electron-ferry along the path of Ni^{2+}-Cr^{4+}/Ni^{3+}-Cr^{6+} and Cr^{3+}-Fe^{4+}, achieving deep activated Ni(Fe)OOH layer with highly stable Fe sites in OER reconstruction process. The reconstructed NiCrP@NiFeP electrode shows 270 mV over-potential at 100 mA cm^{-2} current density with steady working more than 2600 h.

1. Introduction

Electrochemical oxygen evolution reaction (OER) with four-electron-transfer pathway is a fundamental and important half-reaction in photo-/electrocatalytic water electrolyzer, [1–3] and aqueous metal-air batteries [4], but displaying a low kinetics that makes it become the bottleneck restricting the energy efficiency of above-mentioned devices [5]. Developing high efficiency OER catalysts with low-cost and superior durability properties is a key factor to achieve top-performance energy storage and conversion devices [6]. Binary/ternary-transition-metal based catalysts including of metal phosphide/sulfide/nitride/oxide have the adjusted electron filling state in 3d-orbitals, which are expected to become the important candidate materials for OER catalysts [7]. In principle, the strong electron interaction between heterogeneous metal ative centers guides the adsorption of surface-based oxygen intermediates for high oxygen evolution [8]. However, most of the heterogeneous metal atoms is nonadjacent (especially during surface

reconstruction), the high spatial barrier makes it difficult for electron transfer to achieve activated metal centers, limiting the exposure and stability of active sites for enhancing the OER performance.

Despite more and more efforts have been applied on predesigning the OER catalysts with optimized electron structure, [9–12] the electron-transfer path in metal centres always be destruct under electro-oxidation conditions due to the thermodynamic instability of active species. On the one hand, the inevitable dissolution of high-valence active metal ions would breakdown the electron interaction resulting in the inactivation of metal centres. On the other hand, the in situ formed dense reconstruction layer (about 10 nm thick) seriously passivates the surface that restricts the electron exchange with inner metal atoms [13]. In previous studies, loading nanoclusters on the catalyst surface is one of the most effective ways to reconstruct new electron-transfer units in the reconstruction layer [14,15]. For example, Jiande Chen et al. modified FeO_x clusters on the surface of NiFe-LDH to in-situ form the FeOOH//NiFe-LDH interface in OER process for

---

strengthening the binding of $Fe^{(3+\delta)+}$-O-Ni^{2+} units, significantly promotes the oxidation of Ni^{2+} and improve the OER reaction efficiency [15]. Besides, keeping the dynamic equilibrium of surface composition is another effective method for realizing the electron exchange between heterogeneous metal ions. Recently, Nenad M. Markovic constructed a dynamic equilibrium in dissolution-redeposition of Fe^{3+} on the surface of NiFeLDH by inducing 0.1 mg/L Fe^{3+} in electrolytes [16]. Furthermore, Yanbo Li and Ian D. Sharp used Co as an accelerator of Fe^{3+} in-situ deposition strengthen the above equilibrium, realizing a self-healing catalyst for high durability [17]. It is found that the instable components will transformed into thermodynamically stable species during the further reconstruction process. However, these strategies only work in a limited scope on the catalyst surface, most of the metal ions in the reconstruction layer can't be activated.

Nowadays, the underlying reconstruction mechanism in deep activation is still unclear despite the certain recognition of reconstruction chemistry has been achieved, how to improve the amount and stability of active sites is still of a great challenge. During OER, the metal atom migration seriously affect the structure and electron distribution of active units, which is important but always be ignored on the cooperative enhancement effects between active sites. Inducing the orderly release of foreign metals in OER process can not only effectively realize the redistribution of electron cloud around metal sites, but also increase the depth of electrolyte infiltration on electrode surface, which may improve the catalytic activity even further. For example, Al, Cr, Mo elements have been commonly doped and investigated in NiFe based catalysts, in which the addition of Cr displays a better effective in modulating the electrocatalytic activity at the atomic level due to its several oxidation states (from +1 to +6) [18–20]. Among these Cr ions, Cr^{3+} and Cr^{4+} are very common and stable oxidation states, which could be a suitable candidate as electronic carrier to transfer electrons between nonadjacent metal ions.

Here, we developed a new concept of electronic-ferry in metal element migration to bridge the electron-interaction between nonadjacent heterogeneous metal ions, realizing a deep activation of the selected catalyst with synchronously improved OER kinetics and corrosion resistance of metals centres. By designing the layered NiCrP@NiFeP with concentration gradient, the reconstruction process with inner Cr stepwise-release can generation more active Ni(Fe)OOH species. In this process, the electron can be ferried along the path of Ni^{2+}-Cr^{4+}/ Ni^{3+}-Cr^{6+} and Cr^{3+}-Fe^{4+}, endowing the electron-bridge between the nonadjacent Ni and Fe ions to achieve $Ni^{(3+\delta)+}$ with much higher valence state and $Fe^{(3+\delta)+}$ with fast electron recovery capability. Different from the instability of Fe atoms in other NiFe-based catalysts, the surface Fe retention ratio in this work is greatly increase from 28.1 % to 43.8 %, which is benefit for achieving high catalysis durability. After the whole reconstruction process, the NiCrP@NiFeP electrode shows a low OER overpotential of 209 mV at 10 mA cm^{-2} current density. Furthermore, it can continuous stable working for more than 2600 h with only 30 mV decay at 100 mA cm^{-2} of current density at room temperature. In simulated industry conditions (30 wt% KOH, 60.9 °C), the deeply activation of NiCrP@NiFeP electrode enables much higher catalytic durability than other electrodes, which shows the potential to be applied in industry.

2. Experimental section

2.1. Chemicals

All the Chemicals used in this work were purchased from Aladdin Reagent Co., Ltd. Including nickel nitrate hexahydrate (Ni $(NO_3)_2 \cdot 6H_2O$), iron nitrate nonahydrate ($Fe(NO_3)_3 \cdot 9H_2O$), chromic nitrate ($Cr(NO_3)_3 \cdot 9H_2O$), ammonium fluoride (NH_4F), urea ($CO(NH_2)_2$), potassium hydroxide (KOH) and sodium hypophosphite (NaH_2PO_2). Distilled water and ethanol were used for washing and reaction.

2.2. Synthesis of $NiFeP_x$ and $NiFeCrP_x$

First, the precursor Ni_4Fe-LDH grown on Ni foam (2 cm × 3 cm) was prepared by reacting $Ni(NO_3)_2 \cdot 6H_2O$ (3 mmol), $Fe(NO_3)_3 \cdot 9H_2O$ (0.75 mmol), NH_4F (15 mmol) and urea (37.5 mmol) in a hydrothermal reactor at 120 °C for 16 h. Second, the Ni_4Fe-LDH phosphating was processed in tube furnace by H_2/Ar flowing at 300 °C for 2 h, in which NaH_2PO_2 was used as phosphorus source. Then, the $NiFeP_x$ coated Ni foam was synthesized. Besides, the $NiFeCrP_x$ was obtained by using the same method with adjusting the Ni/Cr = 3;1.

2.3. Synthesis of layered NiCrP@NiFeP with concentration gradient

First, the $NiCr$-LDH@Ni_4FeO_x precursor was constructed using a two-step hydrothermal method. $Ni(NO_3)_2 \cdot 6H_2O$ (1 mmol), $Cr(NO_3)_2 \cdot 6H_2O$ (2 mmol) and and urea (10 mmol) were hydrothermal reacted at 120 °C for 6 h with Ni foam (2 cm × 3 cm) as substrate. Then, the obtained sample as substrate was transferred into another hydrothermal process reacting at 120 °C for 16 h, which using $Ni(NO_3)_2 \cdot 6 H_2O$ (0.3 mmol), Fe $(NO_3)_3 \cdot 9H_2O$ (0.075 mmol), NH_4F (1.5 mmol) and urea (3.75 mmol) solution as reactants. The obtained sample is $NiCr$-LDH@Ni_4FeO_x precursor. After the followed phosphating steps, we can obtain the layered NiCrP@NiFeP catalysts with concentration gradient.

2.4. Materials characterization

The phase characterization involved in this paper were performed at X-ray diffraction (XRD, Ultima IV) using Cu Ka radiation (k = 0.15405 nm). The morphological characterization were observed by Scanning electron microscopy (SEM, Nova Nano SEM 450) with a field emission scanning electron microanalyzer, Transmission electron microscopy (TEM, JEM-2100) at 200k eV, and TEM-EDS elemental mapping (Thermo ESCALAB 250XI). The strcture analysis were conducted by X-ray photoelectron spectra (XPS, Escalab 250Xi) using 300 W Al Ka radiation, and Raman spectra (Renishaw inVia).

2.5. Electrochemical characterizations

All electrochemical tests were conducted by three-electrode system with Pt wire as counter electrode and Ag/AgCl as reference electrode on CHI 760e electrochemical workstation. The tested potential for CV is ranged from 0 to 0.8 V versus Ag/AgCl at a scan rate of 10 mV s^{-1}. Lab condition is pH= 14 KOH aqueous electrolyte at room temperature, while the industry condition is 30 wt% KOH solution at 60.9 °C. Besides, the reduction potential of Ni, Fe and Cr ions is tested by CV in $A(NO_3)_x$/ KNO_3 (A=Ni, Cr, Fe) electrolyte with 0.1 M $A(NO_3)_x$ in 1 M KNO_3 solution. CP test is performed at a current density of 100 mA cm^{-2}. The EIS of electrodes was measured from 0.01 to 100 KHz frequency with an applied AC potential of 5 mV. The potential conversion followed the formula: $E_{RHE} = E_{Ag/AgCl} + 0.197 + 0.059 \times pH$.

2.6. DFT calculation

Our calculations were performed using first-principles density functional theory (DFT), as implemented in the Materials Studio 2020. The general gradient approximation of Perdew-Burke-Ernzerhof (GGA-PBE) was used to describe the exchange−correlation (XC) functional. Candidate structures for bulk NiOOH were explored using DFT + U with an effective U−J term of 5.5 eV for Ni 3d state and 3.0 eV for Fe and Cr. For all optimization calculations, the convergence criteria for energy and force were set to 10^{-5} eV and 0.01 eV Å^{-1}, respectively. The cutoff energy was set to 450 eV. The lateral dimension includes 2 × 2 unit cells with 1/3 ratio of Ni sites being occupied by Fe and Cr, respectively. The normal valence/outer-core electrons that are included in the self-consistent-field calculations are listed inter parentheses for each atom: Ni ($3d^8 4s^2$), Fe ($3d^6 4s^2$), C ($2s^2 p^2$), N ($2s^2 p^3$), O ($2s^2 p^4$) and H ($1s^1$).

The adjustment of valence state in metals is completed with the arrangements of the H-atoms in NiOOH.

3. Results and discussion

As one of the cheap and high intrinsic activity candidate electrocatalysts, NiFe-based phosphides experience a serious reconstruction in OER process [21,22]. As shown in Scheme 1a, the surface oxidation of NiFeP would promote the dissolution of Fe^{3+} in alkaline electrolyte, forming a dense active layer that limits the further exposure of the high-valence metal centers, resulting in the low truly activity and stability of NiFeP electrode. Facing this problem, traditional strategies mainly introduce foreign metal elements into active layer to adjust the electron structure as well as to protect metal atoms from dissolution (such as Cr doping NiFeP in Scheme 1b) [23–25]. But the foreign metal would experience a fast leaching before the reconstructed species that reaches thermodynamically stable. Based on our previous research, the foreign metal element can migrate from the bulk phase to surface driven by the chemical potential difference of concentration gradient distribution [26]. Herein, the leaching speed of Cr^{3+} would be further slow down to continuous protect the electron structure of catalysts in the entire surface reconstruction process by designing a layered NiCrP@-NiFeP with Cr in the inner parts (Scheme 1c). Besides, the variable valence state of Cr ions (Cr^{2+}, Cr^{3+}, Cr^{4+} Cr^{6+}) may provide an electron bridge between non-adjacent metal atoms, promoting the activation of metal centers to achieve a much higher efficiency OER performance.

3.1. Characterization of the synthesis NiCrP@NiFeP sample and Its OER activation process

First, the NiCrP@NiFeP catalyst was prepared by a two-step hydrothermal reaction followed by phosphating, which was then characterized by a combination of various techniques. The X-ray powder diffraction (XRD) spectrum of NiCrP@NiFeP reveals that the sample is mainly composed with various low crystallinity NiFe-based phosphides, which would all completely transformed into an amorphous state after OER (Fig. 1a). It is note that no obvious NiCrP phase was detected, which may be caused by the low crystallinity or less distribution on the surface. Analogous results also be found in the XRD spectrum of NiFeCrP and NiFeP before and after OER in Fig. S1. Besides, the surface characteristic of three samples was studied by scanning electron microscopy (SEM), energy dispersive X-ray spectroscopy (EDX) and transmission electron microscopy (TEM). SEM images in Fig. 1b, c and S2 displays 3D-flower structure NiCrP@NiFeP composed by thin nanosheets grown on the Ni foam, the average size is about 5 μm. TEM detection in Fig. 1d shows the micro structure of NiCrP@NiFeP (image 1 and 4), NiFeP (image 2) and NiFeCrP (image 3), respectively. It can be found that the NiFeP epitaxial grown on the NiCrP surface in NiCrP@NiFeP, which is further confirmed by the EDX results (Fig. 1e and Fig. S3). Besides, the X-ray photoelectron spectroscopy (XPS) with in-situ etching of NiCrP@-NiFeP demonstrates a typical concentration gradient distribution of Cr from the bulk to surface (Fig. S4a). HRTEM in image 5 displays obvious (200) and (102) crystallographic plane that is believed corresponding to $Cr_{0.75}Ni_{0.25}P$ phase in NiCrP@NiFeP sample (PDF# 78–0271), though there is no corresponding diffraction peak (33.775° and 34.426) appeared at XRD. Besides, the selected-area diffraction (SAD) in image 6 shows typical polycrystalline structure characteristics of NiCrP@NiFeP, which is consistent with XRD results. Furthermore, the electronic states of the as synthesized NiCrP@NiFeP sample was analyzed by XPS fitting spectra in Fig. 1f. Distinct Ni 2p, Fe 2p and P 2p signals are detected except Cr 2p peak, which means the Cr distribution mainly in the inner part of the sample. In Ni 2p spectra, a distinct $2p_{1/2}$ peak around 874.4 eV and $2p_{3/2}$ peak around 856.5 eV along with a high ratio of Ni^{3+}/Ni^{2+} [18]. Fe 2p can be fitted by a fairly broad Fe $2p_{1/2}$ peak
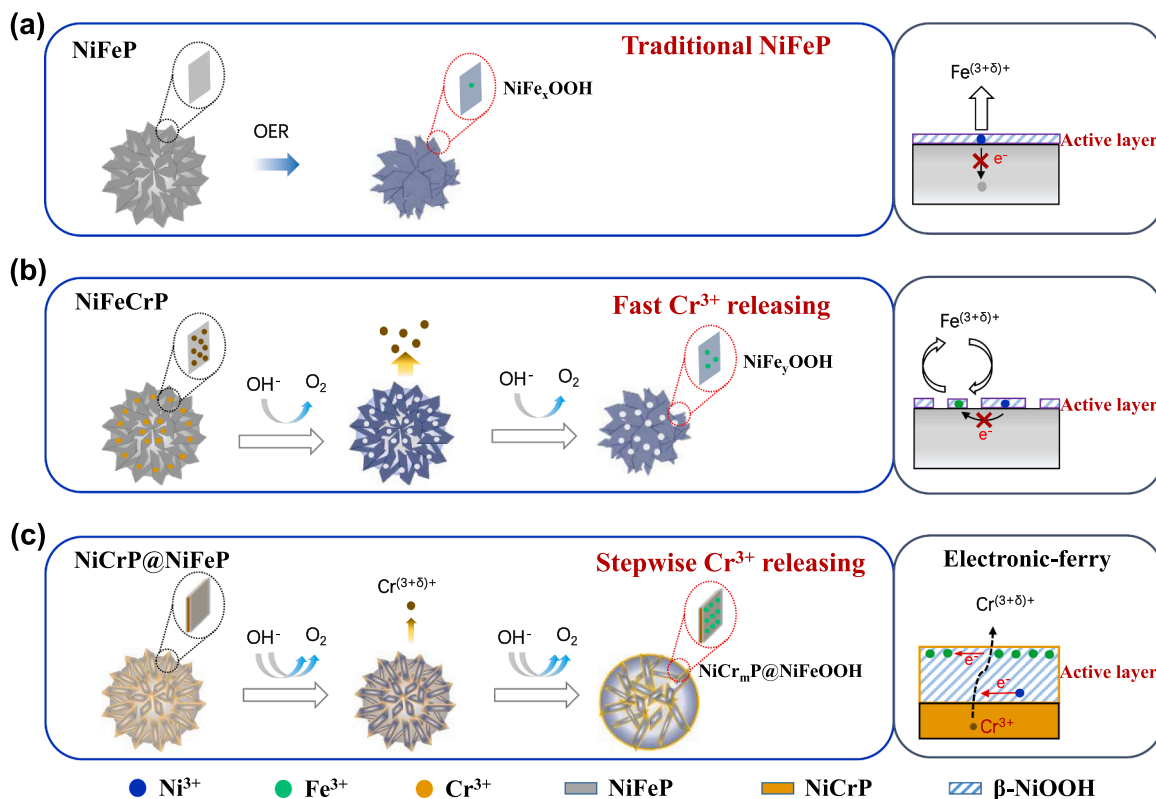
Scheme 1. (a) The surface reconstruction of traditional NiFeP catalysts in OER process, Fe leaching in active layer breaks the electron bridge between Ni/Fe ions. (b) Surface activation of Cr^{3+} doped NiFe-based phosphide in OER process, in which the fast leaching of Cr^{3+} induces spatial separation of Ni/Fe sites. (c) The designed stepwise-release of foreign Cr^{3+} from core parts promotes the deep activation of active layer, which strengthen electronic interaction between Ni and Fe sites.
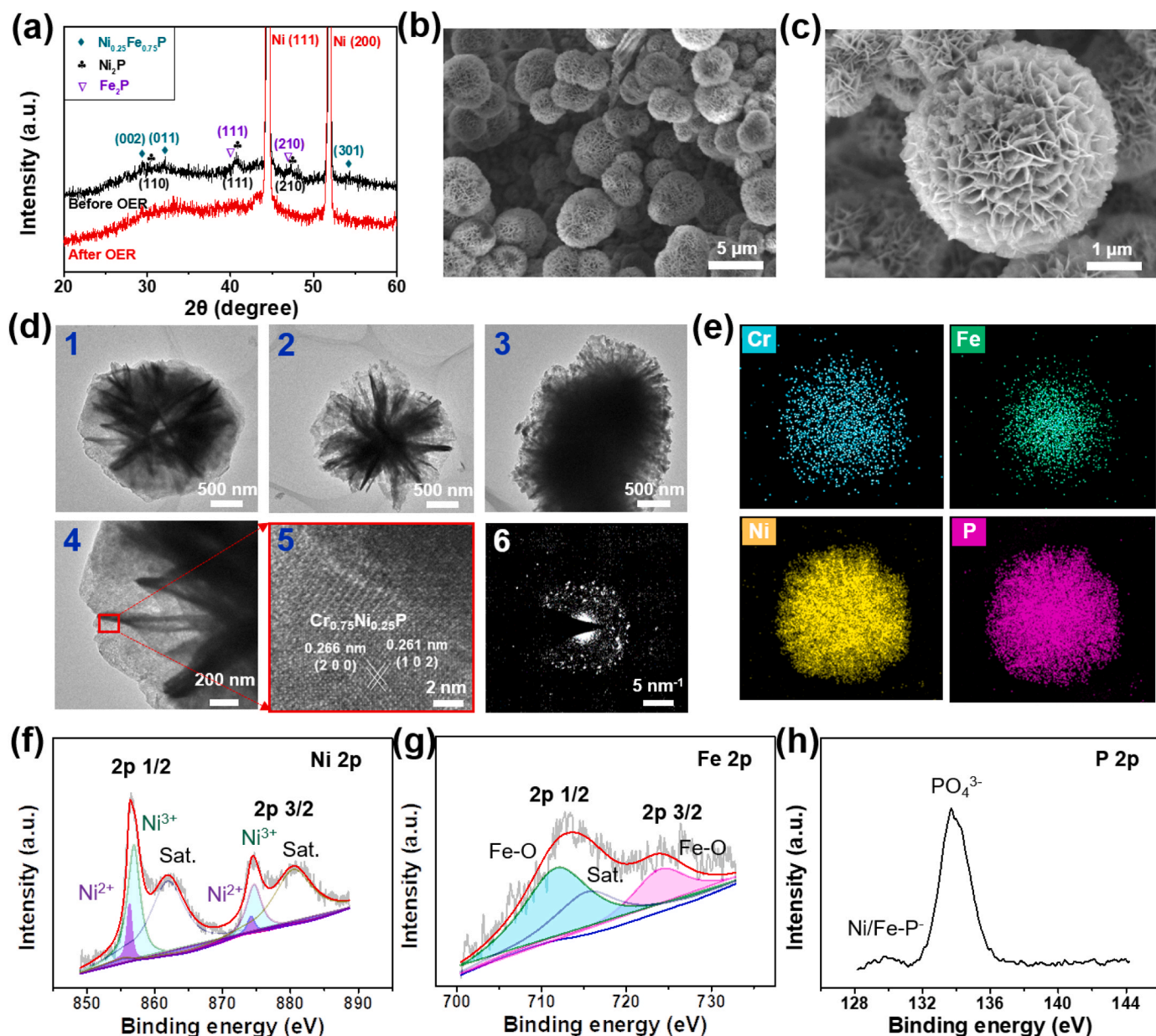
Fig. 1. The structure characterization of NiCrP@NiFeP sample. (a) XRD pattern before and after OER. (b, c) SEM and EDX images of the surface morphology. (d) TEM images of NiCrP@NiFeP (image 1 and 4), NiFeP (image 2) and NiFeCrP (image 3), HRTEM (image 5, PDF# 78-0271) and SAD (image 6) of NiCrP@NiFeP sample. (e) EDX images of NiCrP@NiFeP. (f-h) Fitted XPS spectrum of Ni 2p, Fe 2p and P 2p of NiCrP@NiFeP sample. These results confirm the layered NiCrP@NiFeP with concentration gradient being constructed successfully.

around 711.6 eV and a Fe $2p_{3/2}$ peak around 724 eV along with a small satellite near 718.6 eV that is associated with Fe^{3+} (Fig. 1g) [27]. Besides, P 2p shows a significant PO_4^{3-} peak at 133.2 eV and a small Ni/Fe-P peak at 129.8 eV (Fig. 1h), [28] indicates that both metallic phosphide and phosphate exist on the surface of NiCrP@NiFeP sample. The elemental composition of NiCrP@NiFeP samples and comparative samples are listed in Table S1, further confirming the element composition of Ni, Fe, Cr in NiCrP@NiFeP and NiFeCrP, and Ni, Fe elements in NiFeP. To sum up, the as synthesized NiCrP@NiFeP sample has a layered flower structure with NiFeP epitaxial grown on the surface of NiCrP.

The OER reconstruction process of NiCrP@NiFeP, NiFeCrP and NiFeP were evaluated by CV cycling with the work potential range from 1 to 1.8 V vs. RHE. As shown in Fig. 2a, the redox peaks in the first and 200th CV cycling corresponding to the redox reaction of $Ni^{2+}/Ni^{(3+\delta)+}$, the sharp pre-redox peaks of Ni shifted positively in the potential range of 1.36–1.52 V vs. RHE, suggesting that Ni sites become more difficult to

oxidize into a higher oxidation state due to the phosphide converted to hydroxyl oxide. After the surface construction, the postive electro-activation of NiCrP@NiFeP appears at the first 200 CV cycles and then keep stable, the OER activity has been enhanced by 4 times at 1.5 V vs RHE (from 20.3 to 86.1 mA cm^{-2}), and its overpotential reduces for ~30 mV (reaching 209 mV) at 10 mA cm^{-2} current density without IR compensation. The detailed OER evolution process of the three samples at 0–200th CV cycling are shown in Fig. 2b-c and Fig. S7, in which all the electrodes display different evolution trend of oxidation peaks and overpotentials. The current density of oxidation peaks for NiCrP@NiFeP increases with prolonging the CV cycling, while it presents a volcano-like fashion for NiFeCrP, and nearly unchanges for NiFeP (Fig. 2b). Besides, Fig. 2c demonstrates an opposite change for the overpotentials at 10 mA cm^{-2} by the function of CV cycles. All these results indicate a much deeper activation of metal sites in NiCrP@NiFeP than other two samples to achieve the optimal catalytic performance. The
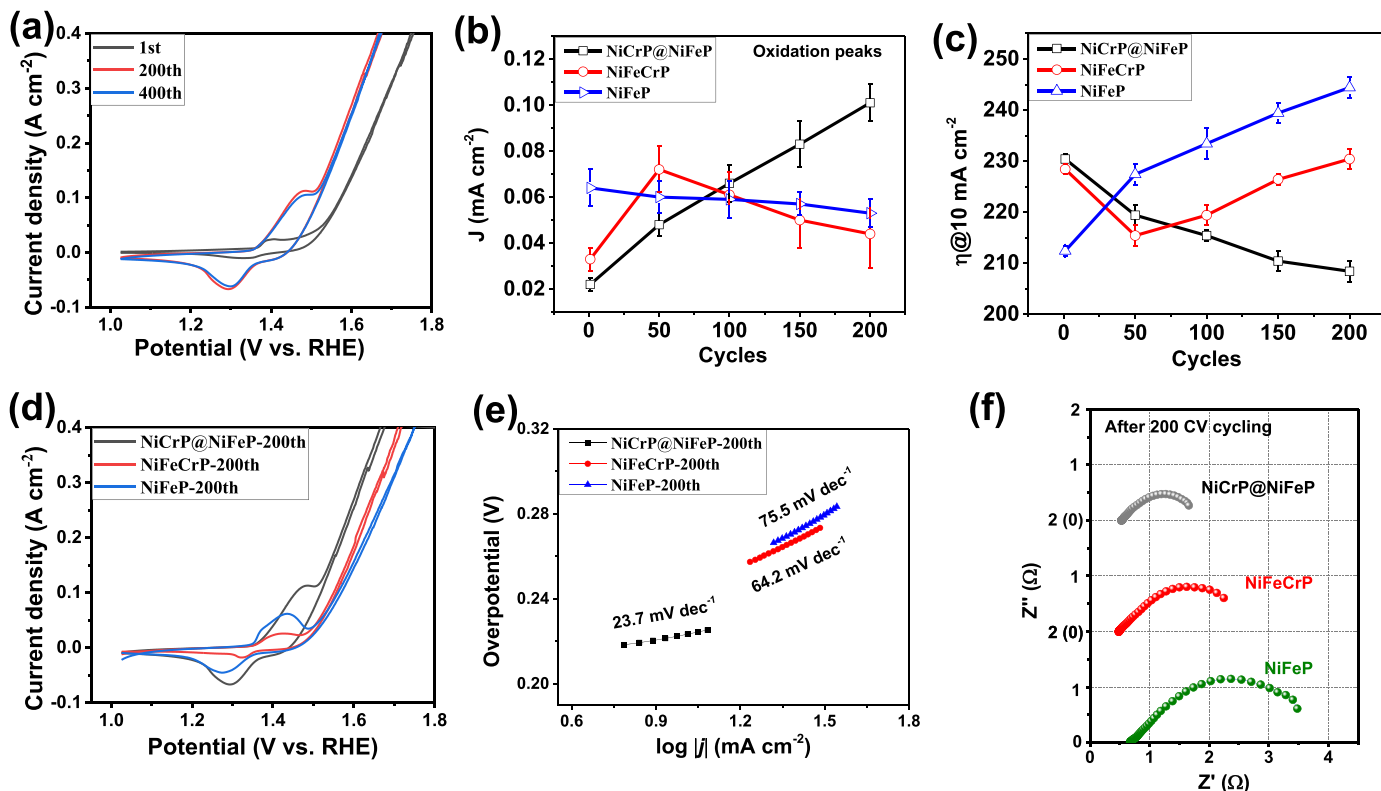
Fig. 2. (a) CV cycles at the scan rate of 10 mV s^{-1} of NiCrP@NiFeP sample. (b) The current density change of oxidation peaks and (c) overpotentials at 10 mA cm^{-2} of NiCrP@NiFeP, NiFeCrP and NiFeP electrodes. (d) CV curves, (e) Tafel slope and (f) EIS of the corresponding three electrodes.

corresponding CV curves, Tafel slope and Electrochemical Impedance Spectroscopy (EIS) of three electrodes after 200 CV cycles (named sample-200th) are shown in Fig. 2d–f, NiCrP@NiFeP-200th shows a significant decrease in Tafel slope (23.7 mV dec^{-1}) and charge transfer resistances (R_{ct}) when compared with NiFeCrP-200th and NiFeP-200th, implies a much better intrinsic OER kinetics for the activated NiCrP@-NiFeP electrodes. Besides, the TEM results in Fig. S9d-f show that the structure of NiCrP@NiFeP changes to ultrathin sheets with low crystalline after OER, which would greatly facilitate the contact of the active site with the electrolyte.

3.2. Stepwise-release of Cr ion promotes the activation of catalytic species

In order to further analyze the essential factors of above phenomenon, we take the XPS and operando Raman measurements to track the species change in the surface of three samples from 1st to 200th CV cycling. As shown in Fig. 3a, the P 2p peak gradually weaken till completely disappeared with CV cycling, which indicates a component reconstruction in electron oxidation process. Fig. 3 b and c present the changes of Cr 2p peaks of NiCrP@NiFeP and NiFeCrP, respectively. For NiCrP@NiFeP sample, no Cr 2p peak signal is detected in initial CV cycles, but it appears after the first 50th CV cycling and then step-weak with prolong the CV cycling. For comparison, the NiFeCrP sample shows a significant Cr 2p peak, which disappeared quickly after 50 CV cycles. The element content ratio of Cr/Fe/Ni in NiFeP, NiFeCrP and NiCrP@-NiFeCrP electrodes at various CV cycles are listed in Table S2. This phenomenon indicates that Cr ions in NiCrP@NiFeP are gradually released from the core to the surface along with the entire OER reconstruction process. Furthermore, the Cr distribution in NiCrP@NiFeP becomes much uniform after 50 CV cycles, confirming obvious Cr element migrating in the OER reconstruction (Fig. S4b). In this process, the Cr element migration promotes the deep activation of the electrode with optimized electron structure, which is proved by the gradual shift of Ni 2p$_{3/2}$ binding energy etching from surface to bulk phase

(0–22.5 nm, **inset images** of Ni 2p spectra). In order to further explore the effect of Cr ion migration on the construction of catalytic active species, we take the operando Raman technology to characterize the structure change of the surface units [29]. The operando Raman spectrum of NiCrP@NiFeP, NiFeCrP and NiFeP at the second CV cycle from 0.1 to 0.7 V vs. Ag/AgCl are shown in Fig. 3d–f, respectively. In Fig. 3d, there is no obvious change of vibration peaks can be detected in NiFeP. While in Fig. 3e, the intensity of Raman peaks centered at 474 and 554 cm^{-1} is improved with positive scanning from 0.5 V to 0.7 V vs. Ag/AgCl, which can be assigned to the E$_g$ bending vibration and A$_{1g}$ stretching vibration of Ni(Fe)-O bond in Ni(Fe)OOH (a mixture of NiOOH and FeOOH, Fig. S12) [23]. The higher 554/474 peak intensity ratio corresponding more β-NiOOH is generated, which is considered to be a more active phase and can be quantified by the operando Raman intensity [30]. At the negative scan from 0.7 V to 0.1 V vs. Ag/AgCl, the above peaks are gradually weaken down finally well recovery to the initial state. For NiCrP@NiFeP in Fig. 3f, the intensity of E$_g$ bending vibration and A$_{1g}$ stretching vibration of Ni-O bonds increased with launching the OER (0–0.7 V vs. Ag/AgCl), while the M-O-Fe vibration (M=Ni and Fe) suffers from a little decrease (nearly unchanged). It displays that the content of Ni -O units in Ni(Fe)OOH is well consistent with the OER activity. Besides, obvious peak split in NiCrP@NiFeP appeared at a much lower potential (0.4 V vs. Ag/AgCl) and the Raman intensity of Ni-O vibrations is much higher than that in NiFeCrP, which is ascribed to the easier formation of para-phase γ-NiOOH in NiCrP@-NiFeP (Fig. S6). It is note that the vibration peak remained high intensity when the voltage was reduced to the initial state, corresponding to a large residual of NiOOH species on the surface of NiCrP@NiFeP. On this basis, the amount of NiOOH gradually increases and reaches to the top after 50 CV cycles, then the intensity ratio of the doublet peaks 554 cm^{-1}/ 475 cm^{-1} increased in the next CV cycling, referring to more active β-NiOOH content (Fig. 3g) [31]. To sum up, the step-release of Cr can realize a deeply activation of the catalysis species in NiCrP@NiFeP sample.
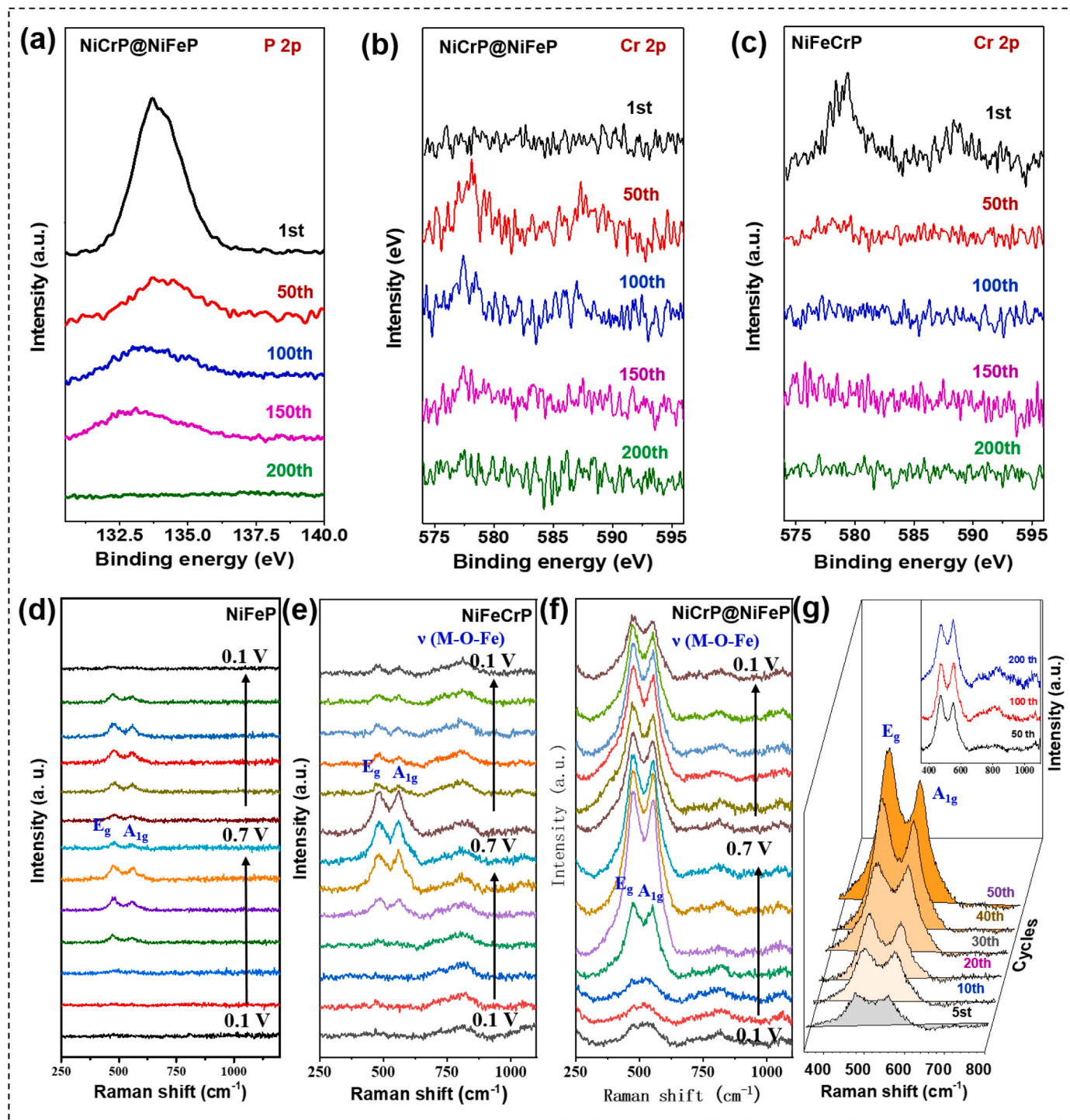
Fig. 3. (a–c) XPS spectrum of the synthesized samples after various CV cycles: (a) P 2p peaks and (b) Cr 2p peaks of NiCrP@NiFeP, (c) Cr 2p peaks of NiFeCrP. (d-f) Operando Raman test of three electrodes in 0.1–0.7 V vs. Ag/AgCl: (d) NiFeP, (e) NiFeCrP and (f) NiCrP@NiFeP. (g) Operando Raman test of NiCrP@NiFeP electrodes with various CV cycles. M=Ni and Fe.

Further to identify the real active sites of NiCrP@NiFeP electrodes, Fig. S13 shows the corresponding XPS spectra at various applied potential (0, 0.42, 0.7 V vs. Ag/AgCl), and NiFeP was used as a reference sample. For NiFeP, the Ni 2p peak sites have little shift (Fig. S13a) even under an applied potential of 0.7 V, while an obvious shift is observed for the Fe 2p peak (Fig. S13b). This result suggests that the majority of oxidation takes place preferentially on the Fe sites in NiFeP. Compared to the selected peak shift in NiFeP, both Ni 2p and Fe 2p peak positive shift in NiCrP@NiFeP during the OER (Fig. S13c, d). In contrast, the Cr

2p peak shows no obvious shift even its intensity decreased in OER (Fig. S13e). This indicates that both Ni and Fe appears more easily to oxidize into higher oxidation state by the surface release of Cr. Based on Xin Bo's research, [31] the increased Cr valence state corresponding to the shorter Cr-O bond, which have an optimal binding capability with the oxygen intermediate during OER. Similar results also be found in NiFeV-OOH catalyst, where a shorter V–O bond was observed and V^{5+} was suggested as the active site [32]. The higher valence state would promote the shorter bonds undergoing continuous fracture and

reconstruction, forming a trap (oxygen vacancy) to absorb OH⁻ during the OER. Herein, Fe sites in NiFeP should be the real active sites in OER, while both Ni and Fe with high valence state in NiCrP@NiFeP catalyst plays an important role on enhancing OER activity. Combining the XPS and Operando Raman results, both the Ni-O and Fe-O bonds with high metal valence state act as the real active sites of NiCrP@NiFeP electrode during OER.

To better understand the changes of the electronic structure in catalyst surface during OER reconstruction, we carried out XPS tracking tests on three samples with different degrees of activation (Fig. 4a–d and Fig. S14). As shown in Fig. 4a and c, both Ni 2p and Fe 2p peaks of NiCrP@NiFeP shift negatively at the first 150th cycles, means the reduction of the average valence for Ni/Fe species. Then, the position of Ni 2p peak keeps stable while Fe 2p peak positive shifts about 1.5 eV when CV cycles to 200th, which is different from NiFeCrP and NiFeP. Due to this trend is strictly consistent with the Cr release process (step-release in 1st −150th and completed from 150th to 200th), we further compare it with NiFeP samples to identify the impact of Cr migration on the change of surface electron structure. As shown in Fig. 4b, the Ni 2p

peaks of NiFeP shifts more negatively during 1–200th CV cycles, indicating Ni ions in NiCrP@NiFeP sample are more prone to oxidation. In Fig. 4d, the position of Fe 2p peak in NiFeP nearly no change in the whole OER process, which means the valence change of Fe ions in NiFeP@NiFeP should be ascribed to the effect of Cr ion migration. Herein, we further explored the metal valence change in NiFeCrP sample. It can be clearly seen that the valence of Fe ion continuous decreased with CV cycling due to the leaching of high valence Fe ions, which can be proved by the most reduced Fe retention in NiFeCrP shown in Fig. 6b. However, the valence of Fe ions in NiFeP@NiFeP fast improved when Cr is completely released (200th), confirming that these Fe ions still have high reactivity after undergoing OER reconstruction. Due to the little leaching of high valence Fe ions on the NiCrP@NiFeP surface in Fig. 6a, the reduced valence of Fe ions between 1st-150th in NiFeP@NiFeP may be ascribed to the capturing of external electrons from the oxidation of Cr^{3+} in the process of Cr release. When the Cr completely leached at 150th-200th, the Fe 2p peak positively shifted under the action of largely formation of ν(Ni-O-Fe), which help stabilize the high valence of Fe. The detail exploration is demonstrated in Fig. S5. Compared the
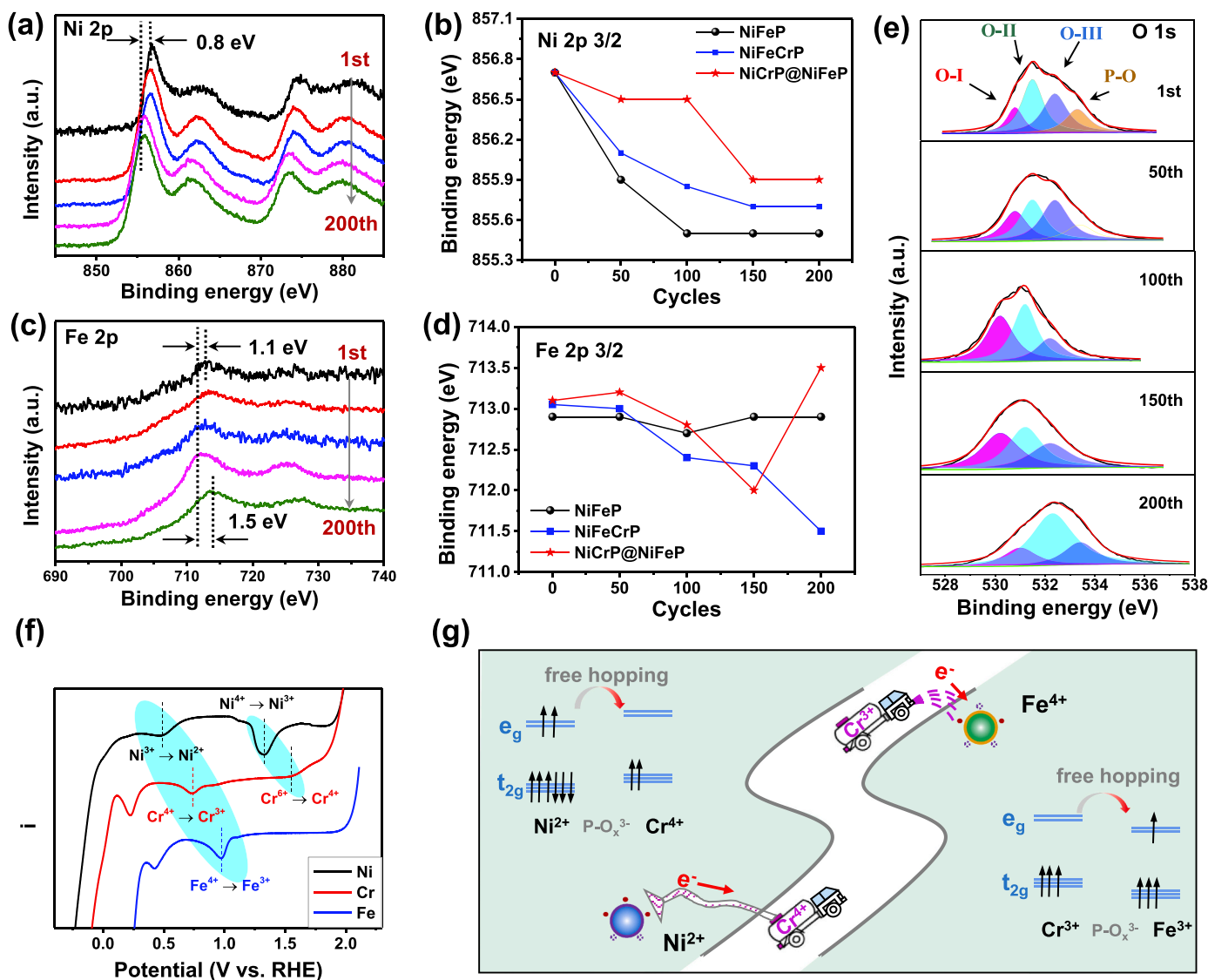

Fig. 4. The detective of electron structure change for three samples in surface reconstruction. (a, c, e) The changes of Ni 2p, Fe 2p and O 1s peaks in XPS spectrum of NiCrP@NiFeP with various CV cycling. (b, d) The comparison of valence state changes corresponding to Ni and Fe ions in three samples along with the CV cycling. The migration of Cr in NiCrP@NiFeP can help improve the valence of Ni ions and strengthen the electron capture ability for Fe ions, while the high valence Fe in NiFeCrP suffers from a serious dissolution. (f) The reduction potential for Ni, Fe and Cr ions in $A(NO_3)_x/KNO_3$ (A=Ni, Cr, Fe) electrolyte. (h) Schematic diagram of the electronic ferry principle in $Ni^{2+}-O-Cr^{4+}$ and $Cr^{3+}-O-Fe^{4+}$ units with Cr^{3+} stepwise-releasing.

whole changes of three electrodes from 1st-200th activation, only NiCrP@NiFeP demonstrates an opposite shift direction of Ni 2p and Fe 2p peaks (Ni 2p peaks negatively shift for 0.8 eV and Fe 2p peaks positive shift for 0.5 eV), indicates that the optimization electron structure has been achieved for NiCrP@NiFeP after reconstruction (named NiCrP@NiFeP-200th). Furthermore, O 1s XPS data of NiCrP@NiFeP shows that the lattice oxygen (O-I) increases and P-O weakens at the first 150th CV cycles (Fig. 4e), which means the oxidation of metallic phosphide with a tight metal-oxide binding thus reducing the Ni/Fe leach in reconstruction process. From 150th to 200th, there is large content of O-vacancies in post-OER catalysts ascribing to the rapid increased valence of Fe ions in the reconstruction process. In Fig. 4f and S15, the reduction potential of Ni, Fe and Cr ions has been evaluated in A $(NO_3)_x/KNO_3$ (A=Ni, Cr, Fe) electrolyte with 0.1 M $A(NO_3)_x$ in 1 M KNO_3 solution. The order of reduction potential for the various metal ions is $Ni^{3+}/Ni^{2+} < Cr^{4+}/Cr^{3+} < Fe^{4+}/Fe^{3+}$ and $Ni^{4+}/Ni^{3+} < Cr^{6+}/Cr^{4+}$, which indicates the electrons would transfer along the path of $Ni^{2+} \rightarrow Cr^{4+} \rightarrow Fe^{4+}$ and $Ni^{3+} \rightarrow Cr^{6+}$ in OER process, so does to both obtain more Ni^{4+} and Fe^{3+}.

To confirm the release process of Cr and its mechanism of action, we further take a DFT calculation to simulate the element migration of Cr and its electron transfer process. The possible Cr migration path in crystalline is assumed along the vacancy and shown in Fig. 5a–d, a unit cell (2 *2) was constructed with 1/3 ratio of Ni sites being occupied by Fe and Cr atoms in NiOOH. We first compare the Gibbs free energies (ΔG) of two different distributions of Fe in the NiOOH, it is found that the energy essentially the same no matter Fe uniform distribution (NiFeOOH-U, Fig. 5a) or occupied on one side (NiFeOOH-S, Fig. 5b). Herein, we choose the NiFeOOH-S to further investigate the trend of Cr migration along the vacancy defect, in which the defect between Fe sites was named V_{Fe}, the defect between Fe sites was named V_{Ni}. By comparing the ΔH of Cr filling in V_{Fe} or V_{Ni} to NiFeOOH-S, the value order is $\Delta H_{VFe} < \Delta H_{VNi} < \Delta H_{NiFeOOH-S}$. Thus, it can be conclude that the Cr trends to spontaneous migrate along the V_{Fe} under the applied electric field. For the electronic-ferry of Cr between Ni and Fe, we construct a unit cell with changed metal valance by adjusting the distribution of H atoms. The theory electron transfer in Ni^{2+}-Cr^{4+} and Cr^{3+}-Fe^{4+} with the visualized electron redistribution is shown in Fig. 5e, f. For group 1, there is evident electron accumulation around Cr and electron lose around Ni, means the Cr^{4+} obtain electron from Ni^{2+} atoms in Ni^{2+}-O-Fe^{3+}-O-Cr^{4+}. For group 2, electron accumulation around Fe and electron lose around Cr, means the Fe^{4+} obtain electron from Cr^{3+} atoms through Fe^{4+}-O-Cr^{3+}. Such a result is constant with the experiment finding in

Fig. 4, confirming the electron transfer in Ni^{2+}-Cr^{4+} and Cr^{3+}-Fe^{4+}. Based on above analysis, such an electronic-ferry mechanism would appear in the activation process of NiCrP@NiFeP catalyst with Cr migration (Fig. 4g), accelerating the formation of high active β-NiOOH species as well as enhancing the corrosion resistance of Fe sites.

3.3. Stepwise-release of Cr ions improves the surface Fe retention for high OER durability

Based on previous reports, the Fe dissolution in NiFe-based catalyst is the critical factor for the deactivation of electrodes [33]. Herein, we first record the atomic ratio in Fe/Ni of NiCrP@NiFeP, NiFeCrP and NiFeP after various CV cycles, respectively. As shown in Fig. 6a, the Fe contention on the surface of NiCrP@NiFeP increases with OER proceed from 0 to 200th CV cycles. DFT calculation in Fig. S8 proves that the Fe-O bond would be strengthen at the first 0–100th due to Cr migration to the surface, hence limiting the high valence Fe leach and increasing the Fe content by phase reconstruction. In contrast, the ratio of Fe/Ni in NiFeCrP sample first increases from 0 to 50th cycles but soon decreases at the followed CV cycles (Fig. 6b), and it decreases at the whole cycling process for NiFeP electrode (Fig. 6c). After surface reconstruction, the atomic ratio in Fe/Ni in NiCrP@NiFeP increases to 43.8 %, but it decreases to 28.1 % and 30.5 % for NiFeCrP and NiFeP. Then, the OER stability of three electrodes was tested by CV cycling, in which NiCrP@NiFeP electrode displays a great stability with nearly no change after 5000 CV cycles (Fig. 6d), but the activity of both NiFeCrP and NiFeP suffer from a serious reduction (Figs. 6e and 5g). From SEM images in Fig. S9a-c, the flower structure of NiCrP@NiFeP changed into fluffy structure coating on the Ni foam after long-time OER, which is caused by the phase transformation from phosphides to oxy-hydroxides. TEM images in Fig. S9g-i displays that the micro-structure of NiCrP@-NiFeP after 5000 CV cycles still keeps the ultrathin sheets with low crystalline. After 5000 CV cycles, ICP-OES results in Table S3 shows that the concentration of Ni and Fe in electrolyte is much lower than Cr, and there is nearly no Ni leaching in long time oxygen evaluation. The stable component in the surface of NiCrP@NiFeP electrode guarantee the high OER stability. When we added trace Fe^{3+} into electrolyte, the stability of NiFeCrP activity is much enhanced (Fig. 6f), while there is little positive effect on NiFeP electrode (Fig. 6h). Thus, the migration of Cr ion can not only improve the corrosion resistance of Fe sites, but also promoting the dissolution-redeposition equilibrium of Fe^{3+} in surface, hence better protect the structural stability of the catalytic species in long-time OER process.
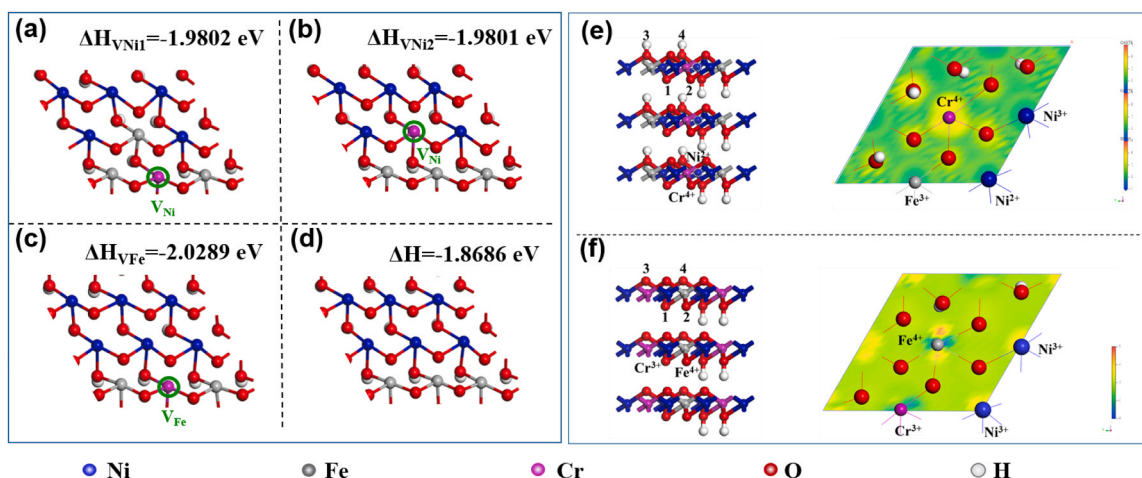

Fig. 5. Comparison of the enthalpy change (ΔH) for Cr occupied various sites. (a) Cr occupied the Ni vacancy with Fe uniform distribution (NiFeOOH-U), (b) Cr occupied the Ni vacancy with Fe distributed on one side (NiFeOOH-S), (c) Cr occupied the Fe vacancy in NiFeOOH-S, (d) pure NiOOH with only Fe doping. The theory electron transfer in (e) Ni^{2+}-Cr^{4+} and (f) Cr^{3+}-Fe^{4+} with the visualized electron redistribution. The Ni^{2+} and Cr^{4+} is bridged by Fe^{3+}, which is obtained by move the H atoms from 1, 2 sites to 3, 4 sites. The Cr^{3+} and Fe^{4+} is adjacent by removing a pair of H atoms from 1 and 2 sites.
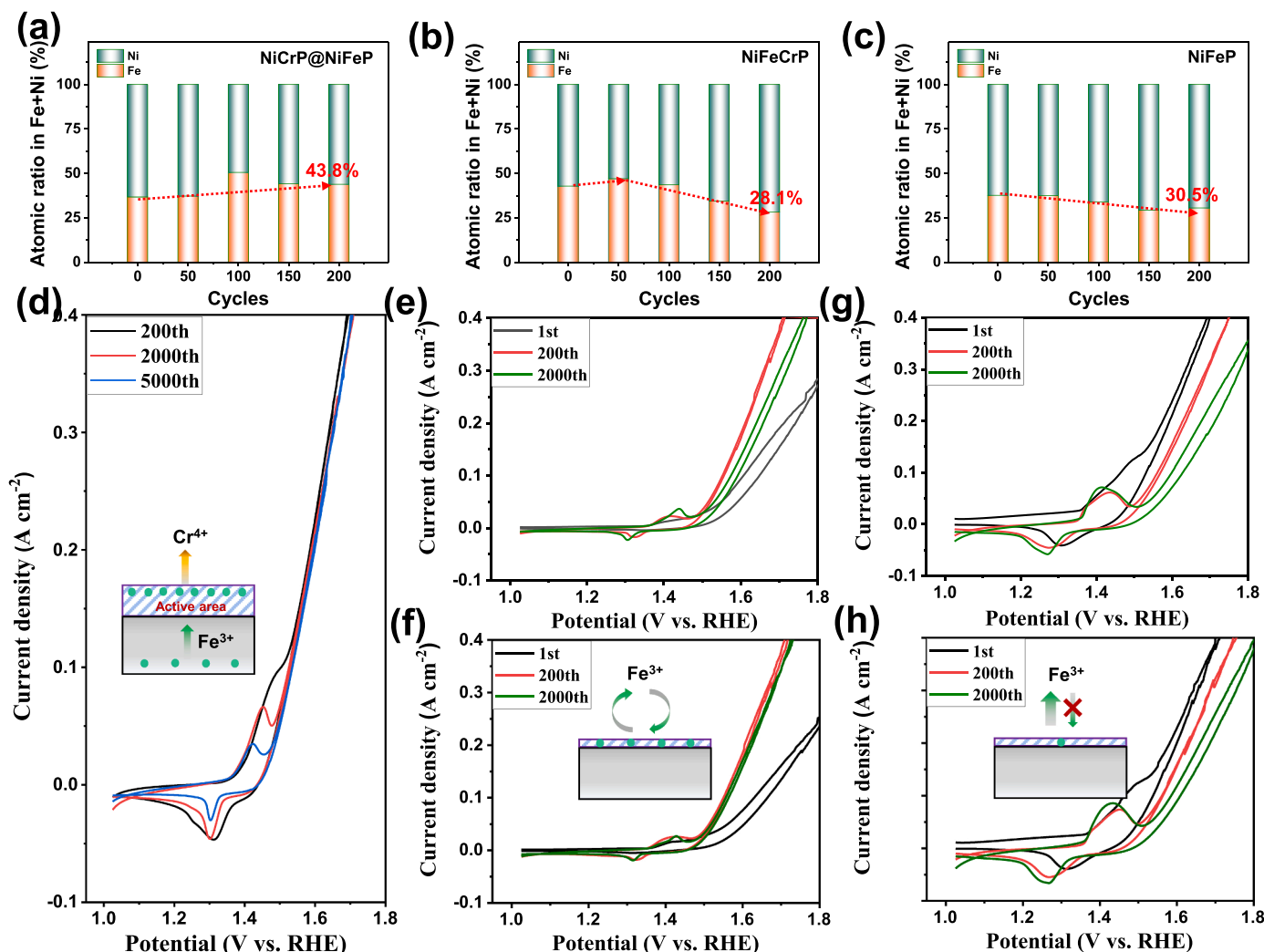
Fig. 6. (a–c) The atomic ratio in Fe/Ni of NiCrP@NiFeP, NiFeCrP and NiFeP after various CV cycles. (d-h) The stability of samples with long time CV cycles: (d) NiCrP@NiFeP, (e) NiFeCrP and (g) NiFeP cycling in 1 M KOH, respectively. (f) NiFeCrP and (h) NiFeP cycling in 1 M KOH+ 0.1 g/L Fe^{3+}, respectively. The insert images in (d, f, h) point to Fe migration in adjacent surface NiFeP region.

Furthermore, we take the chronopotentiometry test at 100 mA cm^{-2} current density in mild condition (1 M KOH, room temperature) to evaluate the long time stability of NiCrP@NiFeP, NiFeCrP and NiFeP electrodes. Fig. 7a shows that the post-activated NiCrP@NiFeP electrode can stable continuous work for more than 2600 h with only small potential fluctuation of ~30 mV, which is much better than NiFeCrP and NiFeP electrodes. After 2600 h test, the electrode transferred into a porous layer structure with disorder atoms arrangement and nearly complete Cr and P release (Fig. S10). In Fig. S11, there is just a little change of the valence state (< 0.25 eV) of Ni and Fe in NiCrP@NiFeP-2600 h compared to that in 200 CV cycles. The high stability of valence state guarantee the long time stable work of electrodes with high performance. Compared with other NiFeCr-based catalysts (<100 h) and NiFe-based phosphides (<1000 h) in previous studies (Table S4), our work exhibits the most stable performance even at the relative higher current density (Fig. 7b). However, there is a gap in evaluating catalyst performance between current studies and industrial conditions (Fig. 7c). To confirm the advantages of the deep activated catalyst in this work, we further evaluated the OER performance of the three activated samples (NiCrP@NiFeP-200th, NiFeCrP-200th and NiFeP-200th) in industry conditions (30 wt% KOH, 60.9 °C) [34,35]. As shown in Fig. 7d, the overpotential of NiCrP@NiFeP-200th is only 150 mV at 100 mA cm^{-2}, while it shows high overpotential about 220 mV and 240 mV for NiFeCrP-200th and NiFeP-200th electrodes, respectively. Besides, the

NiCrP@NiFeP-200th electrode exhibits stable OER for 300 h with 58 mV decay and 230 h with 76 mV decay at 100 and 400 mA cm^{-2}, respectively (Fig. 7e and Fig. S16). These results demonstrate the good catalytic stability and stable active phase of the deep activated NiCrP@NiFeP-200th catalyst under harsh conditions, which is expected to be applied to meet the industrial requirements.

4. Conclusion

In conclusion, an electron-ferry strategy has been performed here to deep activate the NiCrP@NiFeP catalyst by controlling the migration of foreign metal atoms (Cr) in OER process. The oxidized Cr ions capture electrons from Ni ions and transport them to oxidized Fe ions by means of migration, so as to achieve both the increase of active species and the protection of metal sites. After OER reconstruction, the activated NiCrP@NiFeP electrode showed a large increase in Ni(Fe)OOH species and a high retention of Fe/Ni ratio. Herein, the NiCrP@NiFeP electrode shows a low OER overpotential of 270 mV at 100 mA cm^{-2} current density with stable working for more than 2600 h in room temperature. In simulated industry conditions (30 wt% KOH, 60.9 °C), the deeply activation of NiCrP@NiFeP electrode enables much higher catalytic durability than other electrodes, which shows the potential to be applied in industry.
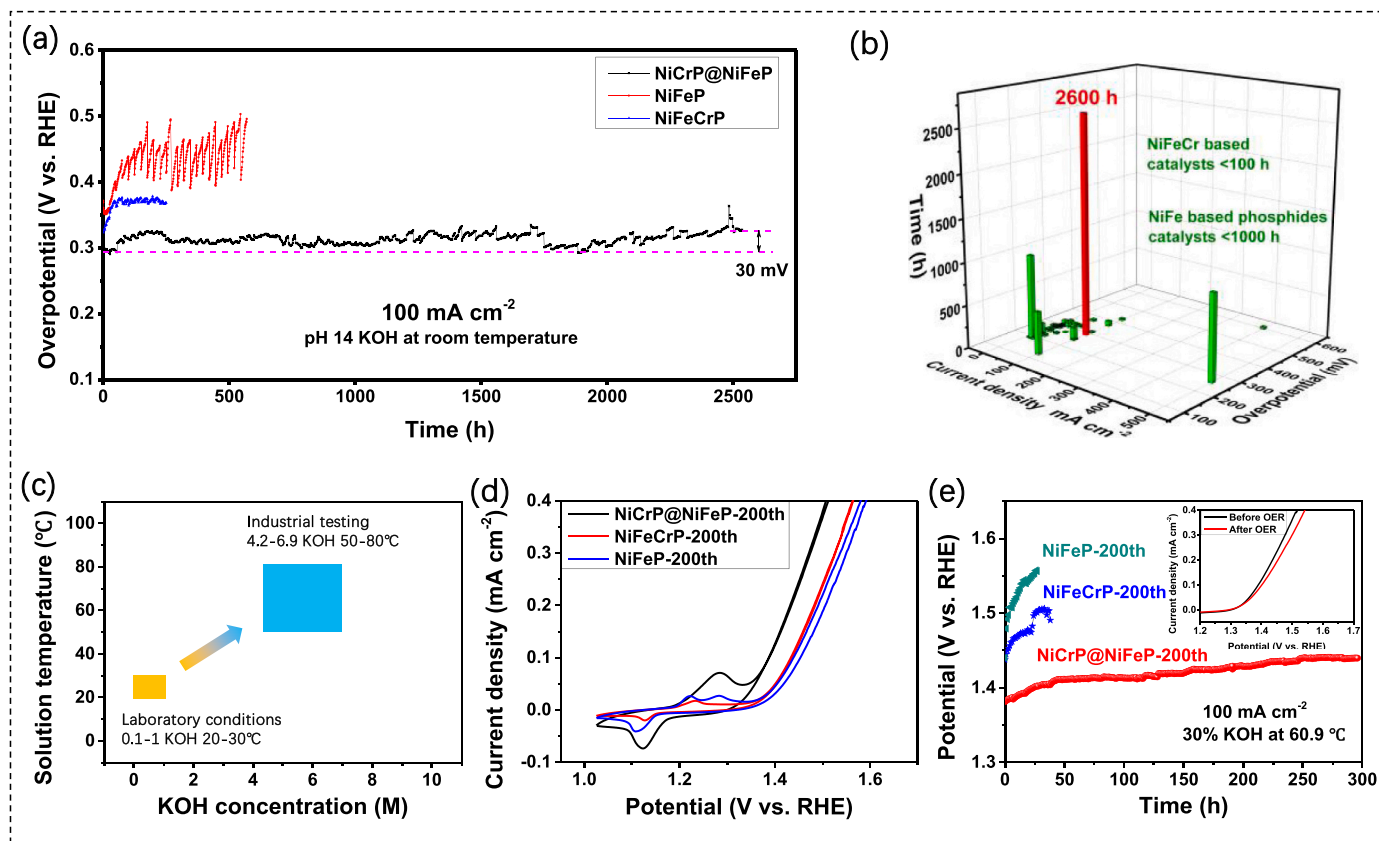
Fig. 7. (a) Chronopotentiometry response of NiCrP@NiFeP, NiFeCrP and NiFeP electrodes at the current density of 100 mA cm^{-2} in pH = 14 KOH, room temperature. (b) The comparison of the stability for the post-activated NiCrP@NiFeP compared with the other NiFe based phosphide electrodes previous reported. (c) The certain gap between traditional test parameters and industrial test parameters. (d) CV test and (e) the long-time stability of the activated electrodes against industrial parameters, 30 wt% KOH at 60.9 °C. Here, the activated electrodes include NiCrP@NiFeP, NiFeCrP and NiFeP after 200-cycle CV activation before chronopotentiometric measurement.

CRediT authorship contribution statement

Xiaobing Wang: Conceptualization, Data curation, Formal analysis, Investigation, Methodology, Writing- original draft, Funding acquisition. **Zhichao Hou:** Data curation, Investigation, Methodology. **Niannian Zhan:** Investigation, Software. **Zhijie Guo:** Supervision, Validation, Review. **Yong Zhao:** Funding acquisition.

Declaration of Competing Interest

The authors declare that they have no known competing financial interests or personal relationships that could have appeared to influence the work reported in this paper.

Data Availability

The data that has been used is confidential.

Appendix A. Supporting information

Supplementary data associated with this article can be found in the online version at doi:10.1016/j.apcatb.2023.123186.

References

[1] Y. Liu, L.J. Wang, H. Zhang, H.Y. Yuan, Q. Zhang, L. Gu, H.F. Wang, P. Hu, P.F. Liu, Z. Jiang, H.G. Yang, Boosting photocatalytic water oxidation over bifunctional Rh^0-Rh^{3+} sites, Angew. Chem. Int. Ed. 60 (2021) 22761–22768.

[2] J. Zhang, J. Cui, S. Eslava, Oxygen evolution catalysts at transition metal oxide photoanodes: their differing roles for solar water splitting, Adv. Energy Mater. 11 (2021) 2003111.

[3] D. Zhao, Z. Zhuang, X. Cao, C. Zhang, Q. Peng, C. Chen, Y. Li, Atomic site electrocatalysts for water splitting, oxygen reduction and selective oxidation, Chem. Soc. Rev. 49 (2020) 2215–2264.

[4] S. Chen, M. Zhang, P. Zou, B. Sun, S. Tao, Historical development and novel concepts on electrolytes for aqueous rechargeable batteries, Energy Environ. Sci. 15 (2022) 1805–1839.

[5] M.F. Lagadec, A. Grimaud, Water electrolysers with closed and open electrochemical systems, Nat. Mater. 19 (2020) 1140–1150.

[6] X. Wang, H. Zhong, S. Xi, W.S.V. Lee, J. Xue, Understanding of oxygen redox in oxygen evolution reaction, Adv. Mater. 34 (2022) 2107956.

[7] Z.-Y. Yu, Y. Duan, X.-Y. Feng, X. Yu, M.-R. Gao, S.-H. Yu, Clean and affordable hydrogen fuel from alkaline water splitting: past, recent progress, and future prospects, Adv. Mater. 33 (2021) 2007100.

[8] Z. Li, J. Yang, Z. Chen, C. Zheng, L.Q. Wei, Y. Yan, H. Hu, M. Wu, Z. Hu, V. Bridged, Co-O to eliminate charge transfer barriers and drive lattice oxygen oxidation during water-splitting, Adv. Funct. Mater. 31 (2021) 2008822.

[9] B. Zhang, L. Wang, Z. Cao, S.M. Kozlov, F.P. García de Arquer, C.T. Dinh, J. Li, Z. Wang, X. Zheng, L. Zhang, Y. Wen, O. Voznyy, R. Comin, P. De Luna, T. Regier, W. Bi, E.E. Alp, C.-W. Pao, L. Zheng, Y. Hu, Y. Ji, Y. Li, Y. Zhang, L. Cavallo, H. Peng, E.H. Sargent, High-valence metals improve oxygen evolution reaction performance by modulating 3d metal oxidation cycle energetics, Nat. Catal. 3 (2020) 985–992.

[10] L. Fan, P. Zhang, B. Zhang, Q. Daniel, B.J.J. Timmer, F. Zhang, L. Sun, 3D core–shell NiFeCr catalyst on a Cu nanoarray for water oxidation: synergy between structural and electronic modulation, ACS Energy Lett. 3 (2018) 2865–2874.

[11] M.-I. Jamesh, M. Harb, Tuning the electronic structure of the earth-abundant electrocatalysts for oxygen evolution reaction (OER) to achieve efficient alkaline water splitting – a review, J. Energy Chem. 56 (2021) 299–342.

[12] J. Mohammed-Ibrahim, H. Moussab, Recent advances on hydrogen production through seawater electrolysis, Mater. Sci. Energy Technol. 3 (2020) 780–807.

[13] X. Liu, J. Meng, J. Zhu, M. Huang, B. Wen, R. Guo, L. Mai, Comprehensive understandings into complete reconstruction of precatalysts: synthesis, applications, and characterizations, Adv. Mater. 33 (2021) 2007344.

[14] W. Yan, Y. Shen, C. An, L. Li, R. Si, C. An, FeOx clusters decorated hcp Ni nanosheets as inverse electrocatalyst to stimulate excellent oxygen evolution performance, Appl. Catal. B-Environ. 284 (2021), 119687.

[15] J. Chen, F. Zheng, S.-J. Zhang, A. Fisher, Y. Zhou, Z. Wang, Y. Li, B.-B. Xu, J.-T. Li, S.-G. Sun, Interfacial interaction between FeOOH and Ni–Fe LDH to modulate the local electronic structure for enhanced OER electrocatalysis, ACS Catal. 8 (2018) 11342–11351.

[16] D.Y. Chung, P.P. Lopes, P. Farinazzo Bergamo Dias Martins, H. He, T. Kawaguchi, P. Zapol, H. You, D. Tripkovic, D. Strmcnik, Y. Zhu, S. Seifert, S. Lee, V. R. Stamenkovic, N.M. Markovic, Dynamic stability of active sites in Hydr(Oxy) Oxides for the oxygen evolution reaction, Nat. Energy 5 (2020) 222–230.

[17] C. Feng, F. Wang, Z. Liu, M. Nakabayashi, Y. Xiao, Q. Zeng, J. Fu, Q. Wu, C. Cui, Y. Han, N. Shibata, K. Domen, I.D. Sharp, Y. Li, A. Self-Healing, Catalyst for electrocatalytic and photoelectrochemical oxygen evolution in highly alkaline conditions, Nat. Commun. 12 (2021) 5980.

[18] Y. Yang, L. Dang, M.J. Shearer, H. Sheng, W. Li, J. Chen, P. Xiao, Y. Zhang, R. J. Hamers, S. Jin, Highly active trimetallic NiFeCr layered double hydroxide electrocatalysts for oxygen evolution reaction, Adv. Energy Mater. 8 (2018) 1703189.

[19] N. Han, F. Zhao, Y. Li, Ultrathin nickel–iron layered double hydroxide nanosheets intercalated with molybdate anions for electrocatalytic water, Oxid., J. Mater. Chem. A 3 (2015) 16348–16353.

[20] F. Liu, Y. Wang, X. Lu, Y. Hu, G. Zhu, R. Chen, L. Ma, H. Zhu, Z. Tie, J. Liu, Z. Jin, The effects of Al substitution and partial dissolution on ultrathin nifeal trinary layered double hydroxide nanosheets for oxygen evolution reaction in alkaline solution, Nano Energy 35 (2017) 350–357.

[21] J. Liu, X. Liu, H. Shi, J. Luo, L. Wang, J. Liang, S. Li, L.-M. Yang, T. Wang, Y. Huang, Q. Li, Breaking the scaling relations of oxygen evolution reaction on amorphous NiFeP nanostructures with enhanced activity for overall seawater splitting, Appl. Catal. B-Environ. 302 (2022), 120862.

[22] L. Gao, X. Cui, C.D. Sewell, J. Li, Z. Lin, Recent advances in activating surface reconstruction for the high-efficiency oxygen evolution reaction, Chem. Soc. Rev. 50 (2021) 8428–8469.

[23] X. Bo, Y. Li, X. Chen, C. Zhao, Operando Raman spectroscopy reveals Cr-induced-phase reconstruction of NiFe and CoFe oxyhydroxides for enhanced electrocatalytic water oxidation, Chem. Mater. 32 (2020) 4303–4311.

[24] Y. Jeung, H. Jung, D. Kim, H. Roh, C. Lim, J.W. Han, K. Yong, 2D-structured V-doped Ni(Co,Fe) phosphides with enhanced charge transfer and reactive sites for highly efficient overall water splitting electrocatalysts, J. Mater. Chem. A 9 (2021) 12203–12213.

[25] Z. Xu, X. Zhang, X. Wang, J. Fang, Y. Zhang, X. Liu, W. Zhu, Y. Yan, Z. Zhuang, Synthesis of Ag–Ni–Fe–P multielemental nanoparticles as bifunctional oxygen reduction/evolution reaction electrocatalysts, ACS Nano 15 (2021) 7131–7138.

[26] C. Wei, N. Heng, Z. Wang, X. Song, Z. Sun, X. Zhu, J. He, Y. Zhao, X. Wang, Dynamic Active Site Evolution and Stabilization of Core-Shell Structure Electrode for Oxygen Evolution Reaction, Chem. Eng. J. 435 (2022), 134672.

[27] H. Liang, A.N. Gandi, C. Xia, M.N. Hedhili, D.H. Anjum, U. Schwingenschlögl, H. N. Alshareef, Amorphous NiFe-OH/NiFeP electrocatalyst fabricated at low temperature for water oxidation applications, ACS Energy Lett. 2 (2017) 1035–1042.

[28] F. Hu, S. Zhu, S. Chen, Y. Li, L. Ma, T. Wu, Y. Zhang, C. Wang, C. Liu, X. Yang, L. Song, X. Yang, Y. Xiong, Amorphous metallic NiFeP: a conductive bulk material achieving high activity for oxygen evolution reaction in both alkaline and acidic media, Adv. Mater. 29 (2017) 1606570.

[29] B.J. Trześniewski, O. Diaz-Morales, D.A. Vermaas, A. Longo, W. Bras, M.T. M. Koper, W.A. Smith, In situ observation of active oxygen species in fe-containing ni-based oxygen evolution catalysts: the effect of pH on electrochemical activity, J. Am. Chem. Soc. 137 (2015) 15112–15121.

[30] T. Chen, B. Li, K. Song, C. Wang, J. Ding, E. Liu, B. Chen, F. He, Defect-activated surface reconstruction: mechanism for triggering the oxygen evolution reaction activity of NiFe phosphide, J. Mater. Chem. A 10 (2022) 22750–22759.

[31] X. Bo, R.K. Hocking, S. Zhou, Y. Li, X. Chen, J. Zhuang, Y. Du, C. Zhao, Capturing the active sites of multimetallic (Oxy)hydroxides for the oxygen evolution reaction, Energy Environ. Sci. 13 (2020) 4225–4237.

[32] J. Jiang, F. Sun, S. Zhou, W. Hu, H. Zhang, J. Dong, Z. Jiang, J. Zhao, J. Li, W. Yan, M. Wang, Atomic-level insight into super-efficient electrocatalytic oxygen evolution on iron and vanadium Co-Doped Nickel (Oxy)hydroxide, Nat. Commun. 9 (2018) 2885.

[33] J. Mohammed-Ibrahim, A review on NiFe-based electrocatalysts for efficient alkaline oxygen evolution reaction, J. Power Sources 448 (2020), 227375.

[34] X. Liu, F. Xia, R. Guo, M. Huang, J. Meng, J. Wu, L. Mai, Ligand and anion Co-leaching induced complete reconstruction of polyoxomolybdate-organic complex oxygen-evolving pre-catalysts, Adv. Funct. Mater. 31 (2021) 2101792.

[35] F. Guo, Y. Wu, H. Chen, Y. Liu, L. Yang, X. Ai, X. Zou, High-performance oxygen evolution electrocatalysis by boronized metal sheets with self-functionalized surfaces, Energy Environ. Sci. 12 (2019) 684–692.